Corrosion Science 183 (2021) 109352

Contents lists available at ScienceDirect

Corrosion Science

journal homepage: www.elsevier.com/locate/corsci

Study on the corrosion behavior of copper coupled with TiO_2 with different crystal structures

Xinyu Zhang [a], Sijia Li [a], Wen Sun [a], Lida Wang [a,*], Jing Wang [b], Guichang Liu [a,*]

[a] School of Chemical Engineering, Dalian University of Technology, Dalian, 116024, PR China
[b] Institute of Oceanology, Chinese Academy of Sciences, Qingdao, 266071, PR China

ARTICLE INFO

Keywords:
TiO_2
Copper
Work function
Oxygen reduction reaction
Corrosion-promotion activity

ABSTRACT

The influences of semi-conductive TiO_2 with different crystal structures on the initial corrosion behavior of copper in dark conditions were investigated. Results showed that anatase TiO_2 showed "corrosion-promotion activity" to copper, while rutile TiO_2 did not. It is revealed that the "corrosion-promotion activity" is associated with TiO_2 crystal structure and mainly dominated by the work function of TiO_2. When the work function of n-type TiO_2 is higher than that of copper, electrons are inclined to transfer from copper to TiO_2. In addition, higher electrical conductivity and oxygen reduction reaction activity of TiO_2 facilitate the electron consumption at the TiO_2/electrolyte interface.

1. Introduction

Semiconductor materials are widely used in various fields such as electrocatalysis [1–4], photocatalysis [5–9], energy storage [10–15] and metal corrosion protection [16–23]. As for applications in corrosion protection, semiconductor materials usually serve as corrosion protective films and coating fillers due to their unique physical and chemical properties, such as high chemical and thermal stability and excellent mechanical properties. Two-dimensional semiconductor materials, such as transition metal dichalcogenides [18], heteroatom-doped graphene [19,21], SnS [24] and so on, possess superior impermeability to molecules and large lateral size, and they can provide outstanding metal protection performance by building physical barriers between metal and reactant. Metal oxide semiconductor materials, such as TiO_2 [25], ZnO [26], Fe_2O_3 [27], Fe_3O_4 [28] and so on, can also enhance physical barrier properties of coatings, depending on their good abrasion resistance and ultraviolet (UV) blocking properties. Besides, another novel application of semiconductor materials is photocathode protection under UV illumination, with semiconductors acting as non-sacrificial anodes [29–32]. In such application, semiconductor materials are coupled with metals such as copper [29,31], carbon steel [30], and 304 stainless steel [32,33]. Semiconductor materials generate photo-generated electron-hole pairs under UV irradiation. The photo-generated electrons in the semiconductor conduction band are transferred to the metal surface with lower potential, resulting in the metal surface potential shifting towards negative direction. Once the metal's surface potential is much lower than its corrosion potential, the metal can be protected from corrosion.

Although semiconductor materials exhibit excellent performance in corrosion protection applications, some recent studies [34–37] indicated that some semiconductor materials showed "corrosion-promotion activity" when they were applied for metal corrosion protection. According to recent research, the titanium-based TiO_2 films prepared by anodization could successfully provide photocathodic protection to carbon steel under UV illumination, but they accelerated the corrosion of carbon steel in the dark [34]. In addition, in our recent work, two semiconducting fillers α-Mn_2O_3 and α-MnO_2 were also found exhibiting intense "corrosion-promoting activity" when they contacted with metals, which was ascribed to their high oxygen reduction activity. Afterward, their "corrosion-promoting activity" was utilized to design novel self-healing systems for metal protection [35,36]. Meanwhile, to demonstrate the corrosion-promotion phenomenon, three typical semiconductor fillers, namely TiO_2, Fe_2O_3 and Cu_2O were chosen to investigate their influences on the corrosion behavior of metal substrates [37]. The experimental results indicated that TiO_2 and Fe_2O_3 tended to accelerate the metal corrosion at the coating defects in darkness or under weak illumination. More importantly, the corrosion-promotion phenomenon was explained as micro-galvanic corrosion between semiconductor and metal, which was attributed to the ohmic contact (n-type anti-blocking layer) at the metal/semiconductor filler interface

* Corresponding authors.
E-mail addresses: ldwang@dlut.edu.cn (L. Wang), gchliu@dlut.edu.cn (G. Liu).

https://doi.org/10.1016/j.corsci.2021.109352
Received 6 April 2020; Received in revised form 13 January 2021; Accepted 26 February 2021
Available online 28 February 2021
0010-938X/© 2021 Elsevier Ltd. All rights reserved.

as well as high oxygen reduction reaction (ORR) catalytic activity of semiconductor fillers. The two main factors are both associated with the intrinsic properties of TiO_2 materials, which are dominated by TiO_2 crystal structures [38–41].

TiO_2 involves several types of crystalline forms, among which anatase and rutile phases are the two most common and stable crystal types. Their structures are both built upon the connection of TiO_6 octahedra. The anatase structure consists of edge-sharing TiO_6 octahedra, while the rutile frameworks exhibit both corner-sharing and edge-sharing configurations [42]. The different crystal structures of the two phases lead to diverse physical properties and electrochemical activities. Meanwhile, many recent theoretical studies indicate that the {001} facet of anatase TiO_2 is much more reactive than the thermodynamically stable {101} surface [38]. The highly reactive facets with high exposure ratio greatly change the physical and chemical properties of TiO_2, such as photocatalytic activity [39], work function [40] and cathodic reaction catalytic activity [41].

The corrosion evolution process of metals can be divided into two stages: initial corrosion stage and subsequent corrosion stage. At the initial corrosion stage, no corrosion products are deposited on the metal surface, while at the subsequent corrosion stage, the metal surface is covered by corrosion products. Therefore, to eliminate the influence of corrosion products on metal corrosion behavior as much as possible, the initial corrosion stage of copper was chosen as the focus of research. To investigate the influences of TiO_2 materials on the copper corrosion behavior at the initial corrosion stage in dark conditions, we chose three kinds of TiO_2 materials (including rutile TiO_2 microsphere, anatase TiO_2 microsphere, and anatase TiO_2 nanosheet with exposed {001} facets). These three kinds of TiO_2 were used to study how the crystal structures of TiO_2 materials affect the initial corrosion behavior of copper when they contact with copper at coating defects. In addition to traditional electrochemical impedance spectroscopy (EIS) measurements, localized EIS (LEIS) measurement is applied to study the interfacial impedance and localized corrosion behaviors of copper/TiO_2 interface with a high spatial resolution at a mesoscale. Besides, scanning Kelvin probe (SKP) measurement and Mott-Schottky measurement are also combined with electrochemical analysis to systematically investigate the corrosion mechanism between semiconductor and metal. This work provides insights into how intrinsic properties of semiconductor (such as crystal structure) affect the "corrosion-promotion activity" of semiconductor materials, which holds promise for the selection and design of suitable anticorrosive materials.

2. Experimental

2.1. Materials and chemicals

Titanium sulfate ($Ti(SO_4)_2$), carbamide ($CO(NH_2)_2$), hydrofluoric acid (HF, 40 wt.%), tetrabutyl titanate (98 wt.%), methanol, and acetone were purchased from Kermel Chemical Reagent Co., Ltd (Tianjin, China). Polyvinyl butyral (PVB) was obtained from Sinopharm Chemical Reagent Co., Ltd (Shanghai, China). All reagents were used without further purification.

2.2. Synthesis of TiO_2 crystals

TiO_2 materials with different crystal structures were synthesized by substituting reactants and controlling different preparation conditions such as reaction time and temperature. In typical anatase TiO_2 microsphere synthesis [37], 4.8 g $Ti(SO_4)_2$ and 12 g $CO(NH_2)_2$ were added into 100 mL Teflon-lined stainless steel autoclave containing 50 mL deionized water under magnetic stirring. Afterward, the autoclave was kept at 130 °C in an oven for 4 h, then cooled down to room temperature naturally. The obtained white precipitates were washed with deionized water and ethanol several times by centrifugation until SO_4^{2-} could not be detected from the supernatant, and then dried in vacuum at 70 °C. The rutile TiO_2 microsphere was prepared by directly calcining the as-prepared anatase TiO_2 microsphere in the air at 900 °C for 3 h using a muffle furnace. The anatase TiO_2 nanosheets with exposed {001} facets were synthesized in the same way as described in the literature [43]. Tetrabutyl titanate (98 wt.%, 10 mL) was dropped one by one into 3.0 mL of HF, under magnetic stirring. The obtained mixture was stirred for 10 min before being transferred into a 50 mL Teflon-lined stainless-steel autoclave. The autoclave was loaded into an oven at 200 °C for 24 h. After the reaction, the anatase TiO_2 nanosheet precipitates were collected, and then washed thoroughly with deionized water and absolute ethanol several times, and finally dried in vacuum at 50 °C.

2.3. Preparation of coatings and electrodes

In the work, to study the effect of TiO_2 on the corrosion behavior of copper, TiO_2 particles were fixed on the copper substrate using PVB binder. For the preparation of TiO_2/PVB coatings, 0.5 g of either of the three types of TiO_2 crystals was added into 8 g methanol, and then stirred for 24 h to give homogeneous mixtures. Subsequently, 1 g PVB powders were added into the mixtures under vigorous stirring, yielding white viscous mixtures with uniformly dispersed TiO_2. The pigment volume concentration of TiO_2/PVB coating was calculated according to the following equation [44]:

$$Pigmentvolumeconcentration = \frac{V_{\text{pigment}}}{V_{\text{binder}} + V_{\text{pigment}}} \times 100\% \quad (1)$$

The calculation revealed that the pigment volume concentrations of three types of TiO_2/PVB coatings were all 11.76 % at the pigment/binder ratio of 1/2. Besides, a pure PVB coating was also prepared for control experiments. Finally, four kinds of PVB coatings were obtained, namely anatase TiO_2 microsphere/PVB coating, rutile TiO_2 microsphere/PVB coating, anatase TiO_2 nanosheet/PVB coating and pure PVB coating.

Fabrication of electrodes: copper substrates were embedded in epoxy resin, leaving a non-resin covered square area of 1 cm^2. The substrates were sequentially polished by 800, 1000 and 1500 SiC grit papers, then sonicated in acetone for 10 min and rinsed with distilled water. After that, the dip-coating method [45] was employed to prepare coatings on the pretreated copper substrates. After immersed in the as-prepared TiO_2/PVB mixtures for 30 s, the copper substrates were vertically lifted at a rate of 6 cm min^{-1} to remove excess coating. The specimens were then dried in air at room temperature for 24 h. The thicknesses of the coatings were measured by using a portable thickness gauge (TR110, Beijing Time High Technology Ltd., China). The thicknesses of the prepared coatings were controlled to be 30 ± 1.5 μm. To study the influences of TiO_2 crystals on the corrosion behavior of copper substrates at the scratches of coatings, an artificial defect with dimensions of 10 × (0.2 ± 0.01) mm was made using a scribing machine.

2.4. Materials characterization

The crystal structure and phase purity of the synthesized TiO_2 were identified by the X-ray diffraction using an X-ray diffractometer (XRD, Empyrean PANalytical, Netherlands) with Cu Kα (λ =0.15418 nm) radiation from 20° to 80° at a scanning speed of 3° min^{-1}. The morphology of the synthesized TiO_2 crystals was characterized by field emission scanning electron microscopy (FE-SEM, ZEISS Ultra 55, Germany) operating at 15 kV. A small portion of TiO_2 samples was spread on the bullseye part of the sample stage with a carbon conductive double-sided tape. After that, blew the sample stage with a rubber ball to sweep away the unstable powder and to make the powder distribute on tape uniformly. Then a conductive layer was deposited on the samples by steaming gold. Finally, the samples could be observed with SEM. Transmission electron microscope (TEM) images and selected area electron diffraction (SAED) of the as-prepared anatase TiO_2 nanosheet with exposed {001} facets were observed on high-resolution

transmission electron microscopy (HRTEM, FEI, Tecnai G2F30, USA) operating at 200 kV. TEM sample was prepared by the deposition of a drop of ultrasonicated and diluted ethanol suspensions on a carbon-coated copper grid with irregular holes.

2.5. Electrochemical measurements

All electrochemical measurements were performed at room temperature in dark conditions. The EIS, Mott-Schottky and ORR measurements were conducted using a CHI750E electrochemical workstation (Chenhua, China) with a conventional three-electrode cell, where a platinum (Pt) plate and a saturated calomel electrode (SCE) were used as the counter electrode and reference electrode, respectively.

The EIS measurements were conducted using a conventional three-electrode cell, where the scratched coated specimens were studied as working electrodes. After the working electrodes were immersed in a 3.5 wt.% NaCl solution for 12 h, the EIS measurements were carried out at the open-circuit potential of the working electrodes, with a sinewave disturbance amplitude of ±10 mV and a frequency range from 10^5 to 10^{-2} Hz.

The LEIS measurements were used to study the local impedance in the presence of the artificial defect using M470 scanning electrochemical workstation (Bio-logic, France). A five-electrode cell was used with the scratched coated specimen as the working electrode, an SCE as the reference electrode, a platinum wire ring as the counter electrode and a LEIS probe as a dual-element probe with the two platinum probes. After immersing the working electrode in a 3.5 wt.% NaCl solution for 1 h, LEIS experiments were done at the open circuit potential with a potential amplitude of ±10 mV and a single frequency of 1 Hz. The distance between the bi-electrode and the working electrode was controlled to ~100 μm, and the scan dimensions were 2 × 2 mm, crossing the artificial defect. The step sizes were 200 μm in the x and y directions.

The work function measurements were carried out using a scanning Kelvin probe (M470, Bio-logic, France) in the air at 25 °C and with a relative humidity of 60 % [46,47]. One hundred micrograms of TiO_2 materials were dispersed in 2 mL ethanol by ultrasonic for 10 min. Then, a 100 μL mixture was coated evenly on the surface of copper electrode (10 × 10 mm, the copper was sequentially polished by 800, 1000 and 1500 SiC grit papers before coating) and dried at 40 °C. After that, the coated electrode was transferred into the chamber of the SKP for the contact potential difference measurements. Meanwhile, the polished copper was also measured by SKP to compare the work function between copper and different TiO_2 materials. The Kelvin probe was made of tungsten with a tip diameter of 500 μm. The distance between the probe tip and the scanning surface was approximately 100 μm. The vibration amplitude was 30 μm and the vibration frequency was set at 80 Hz. The SKP scanning dimensions were 2 × 2 mm with 100 μm step length.

Mott-Schottky plots were measured in a 3.5 wt.% NaCl solution at the fixed frequency of 1 kHz with the applied potential ranging from -0.6 to 0.8 V vs. SCE and an AC voltage magnitude of ±10 mV. In this measurement, the working electrode was fabricated by evenly depositing the TiO_2 onto the surface of the fluorine-doped tin oxide (FTO) conductive glass. Prior to the deposition of TiO_2, the FTO glass (15 × 10 mm) was sonicated in acetone for 10 min and rinsed with distilled water, and subsequently dried with clean airflow. One edge of the long conductive side of FTO glass was covered with insulating tape, exposing a square area of 1 cm^2. One hundred milligram TiO_2 was mixed with 1 mL distilled water and 1 mL ethanol in an agate mortar and the mixture was carefully ground for 5 min to form slurry. Then, 0.1 mL (~5 mg TiO_2) of the as-prepared slurry was evenly spread over the exposed area of conductive side of the FTO glass. After the slurry had dried at 40 °C, the insulting tape was removed. Finally, the FTO glass deposited with TiO_2 was heated to 300 °C for 2 h to improve the adhesion of TiO_2 on the FTO glass. A copper wire was connected to the uncoated part of conductive side of the FTO glass with conductive silver paste. Only the coated area was in contact with the electrolyte during the measurement.

The electrochemical ORR measurements on a glass-carbon rotating disk electrode (RDE, 5 mm diameter, PINE Instrument, USA) were performed with a three-electrode cell in O_2-saturated 3.5 wt.% NaCl solution. For the preparation of the working electrode, 10 mg TiO_2 was dispersed in a 1 mL mixture of water, ethanol and Nafion (5 wt.%, Dupont) ($Vol_{water} : Vol_{ethanol} : Vol_{Nafion} = 5:5:0.1$) by sonication. A 10 μL mixed solution was dropped to the glass-carbon disk. The electrodes were then dried for 30 min at room temperature before measurement. The potential was cathodically scanned between −1.0 and 0.2 V vs. SCE with a scan rate of 10 $mV \cdot s^{-1}$ at 1200 rpm.

3. Results and discussion

3.1. Characterizations of TiO_2 crystals

The crystal structures and morphologies of the as-prepared samples were analyzed by XRD and HR-SEM, respectively, as shown in Fig. 1. Fig. 1**a** shows the XRD pattern of the as-prepared anatase TiO_2 microsphere. The characteristic peaks can be indexed well to anatase TiO_2 (JCPDS No. 21-1272) and no impurity phase is detected. The corresponding SEM image, as shown in Fig. 1b, reveals that the diameter of anatase TiO_2 microsphere is between 0.5 and 4 μm. The XRD pattern of the as-prepared rutile TiO_2 microsphere is shown in Fig. 1**c**. All strong and sharp diffraction peaks are perfectly indexed to rutile TiO_2 (JCPDS No. 21-1276), confirming the pure rutile TiO_2 phase with high crystallinity. By comparing Fig. 1a with Fig. 1**b**, it can be seen that the rutile TiO_2 obtained by calcination still maintains the microsphere structure with a diameter between 0.5 and 4 μm, but its surface becomes smoother. Fig. 1**e** indicates the XRD pattern of anatase TiO_2 nanosheet sample obtained from hydrothermal process in the presence of HF. The diffraction peaks can be successfully indexed to anatase TiO_2 (JCPDS No. 21-1272) with a series of (101), (004), (103), (112), (200), (105), (201) and (215) planes, suggesting a high phase purity for the achieved TiO_2 nanosheet. The relative peak intensity ratio of I(004) : I(101) was calculated to be 27:100, which was larger than the standard value (I(004) : I(101) = 20:100) in the JCPDS No. 21-1272, indicating the predominant exposure of {001} facet [48]. From the insets in Fig. 1f, the anatase TiO_2 nanosheet sample is with an average length of 225 nm and an average thickness of 17.4 nm. TEM was employed to further confirm the exposed crystal facets of anatase TiO_2 nanosheets. Fig. 2**a** shows the TEM image of anatase TiO_2 nanosheets. The corresponding SAED pattern of the selected area (inset in Fig. 2b) which is indexed as the [001] zone axis diffraction confirms that these anatase TiO_2 crystal nanosheets have the representative single crystal characteristics and the faceted surface is the (001) surface [49,50]. The corresponding HRTEM image (Fig. 2b) shows the (200) and (020) atomic planes with a lattice spacing of 0.19 nm and an interfacial angle of 90°, further indicating that the exposed crystal facet is indeed the {001} facet [49,51]. Based on the above structural information, the percentage of {001} facets of the anatase TiO_2 nanosheets was estimated to be ~85.1 %, according to the calculation method of in the literature [51].

3.2. Corrosion behavior of copper coupled with TiO_2 materials

The corrosion behaviors of copper substrates which contacted with TiO_2 were studied using the scratched coated specimens with EIS and LEIS measurements. Fig. 3 shows the EIS results of the scratched coated specimens. After immersed in 3.5 wt.% NaCl aqueous solution for 12 h, the Bode-phase plots of the four scratched coated specimens mainly show two time constants. The high frequency time constant can be ascribed to the copper oxide film and the low frequency time constant to the double layer. The EIS results were analyzed by ZSimpWin software using the equivalent circuit model R(QR)(QR) inserted in Fig. 3a, and the solid lines in Fig. 3**a** and **b** indicate the fitted curves. Herein, R_s is the solution resistance, R_{oxide} and CPE_{oxide} represent the resistance and the capacitance components of the copper oxide film, R_{ct} and CPE_{dl} are the

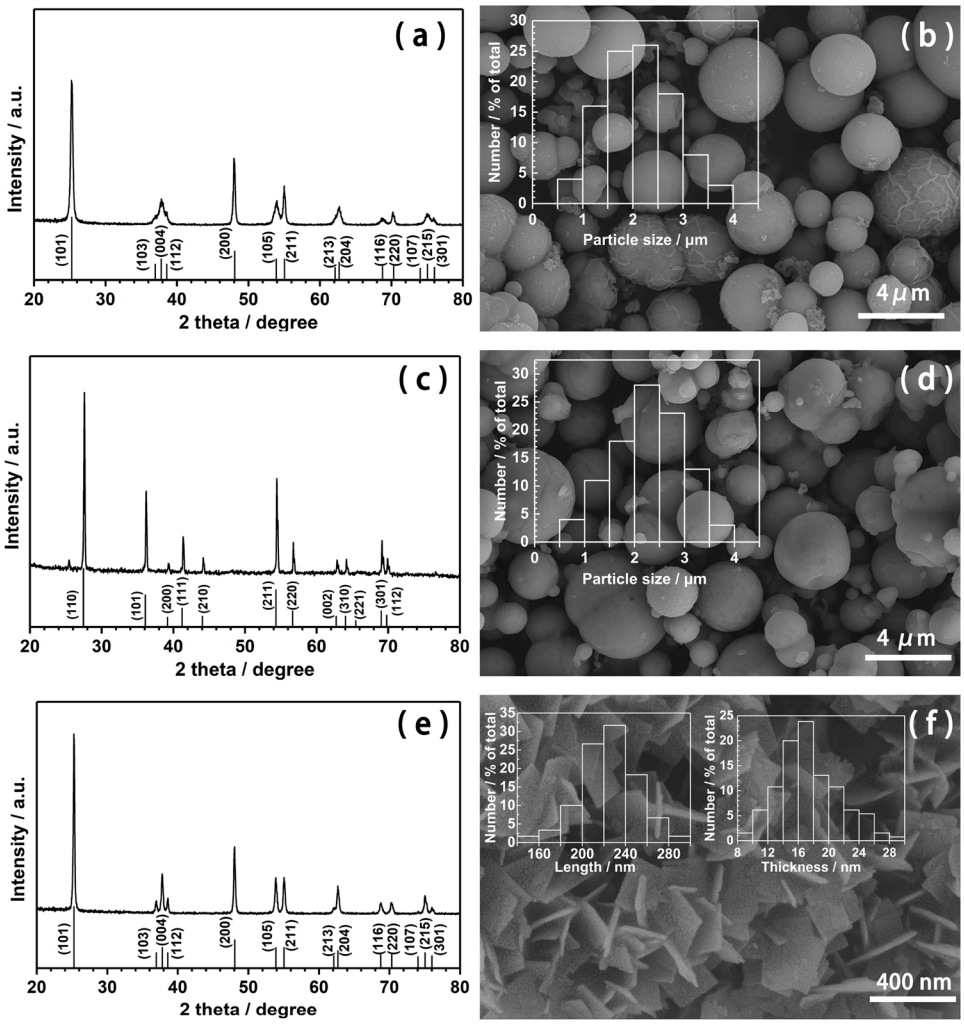

Fig. 1. XRD patterns of (a) anatase TiO_2 microspheres, (c) rutile TiO_2 microspheres and (e) anatase TiO_2 nanosheets and the corresponding HR-SEM images (b), (d) and (f). The insets are the corresponding size distributions.

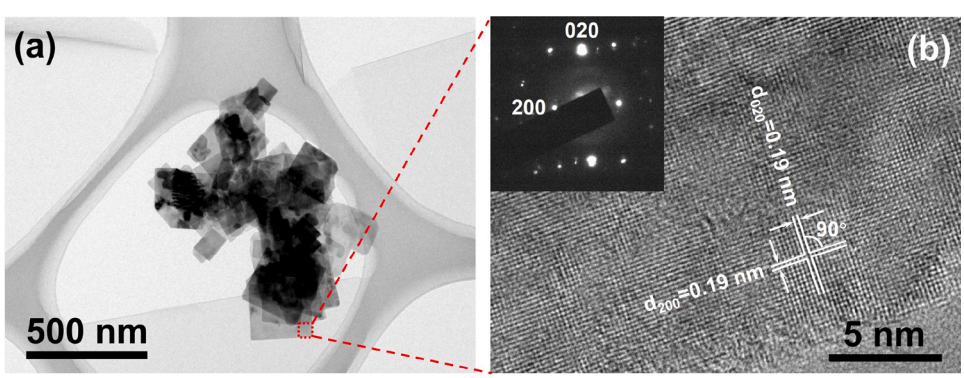

Fig. 2. (a) TEM image of anatase TiO_2 nanosheets; (b) HRTEM image of anatase TiO_2 nanosheets with [001] orientation; the inset shows the corresponding SAED pattern.

resistance and the capacitance components of the electrical double layer, respectively. The quantitative results EIS fitting parameters are provided in Table 1. For the substrates coated by pure PVB coating and rutile TiO_2 microsphere/PVB coating, the values of R_{ct} after immersion for 12 h are about $4.97 \times 10^4\ \Omega\cdot cm^2$ and $4.81 \times 10^4\ \Omega\ cm^2$, respectively, proving that the corrosion resistance of the two scratched coated specimens is similar. However, the R_{ct} value of pure PVB coating specimen is about 16 times larger than that of anatase TiO_2 microsphere/PVB coating specimen ($3.10 \times 10^3\ \Omega\ cm^2$) and 22 times larger than that of anatase TiO_2 nanosheet/PVB coating specimen ($2.25 \times 10^3\ \Omega\ cm^2$). The results quantitatively indicates that the two types of anatase TiO_2 would accelerate the electron transfer process at the interfaces between copper substrate and TiO_2 fillers. The EIS results reveal that the copper substrates which contacted with anatase TiO_2 suffered more severe corrosion than that beneath pure PVB coating. It can be preliminarily deduced that anatase TiO_2 tends to accelerate the corrosion of copper substrates

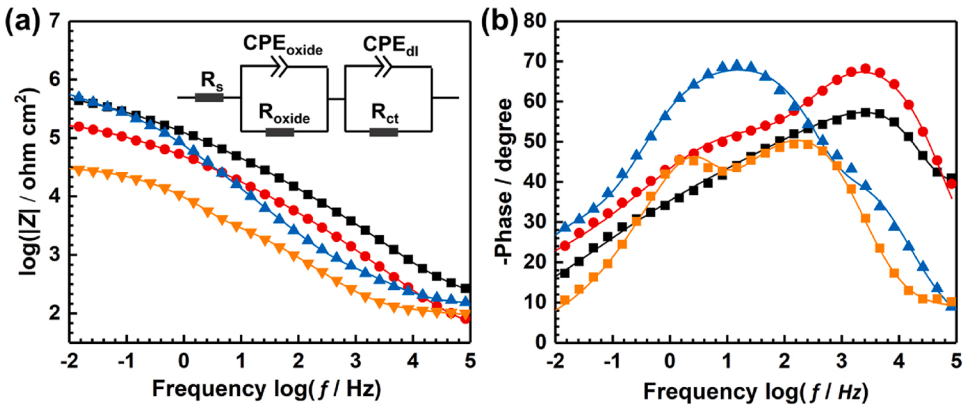

Fig. 3. (a) (b) Bode plots of the four types of coatings immersed in 3.5 wt.% NaCl aqueous solution for 12 h; the inset shows the equivalent circuit model R(QR)(QR) used for EIS data fitting. "■", "●", "▲" and "▼" represent the original Bode plots of pure PVB coating specimen, anatase TiO_2 microsphere/PVB coating specimen, rutile TiO_2 microsphere/PVB coating specimen and anatase TiO_2 nanosheet/PVB coating specimen, respectively. The solid lines represent the corresponding fitted Bode plots.

Table 1
Fitted EIS parameters deduced from Fig. 3 using the equivalent circuit model R(QR)(QR). The unit of resistance is $\Omega\cdot cm^2$, and the unit of Y is $\mu F\cdot cm^{-2}\cdot s^{n-1}$.

Specimens	R_s	R_{oxide}	CPE_{oxide}		R_{ct}	CPE_{dl}	
			Y_0	n		Y_0	n
Pure PVB coating specimen	86.9	6179	2.61	0.65	49,670	3.98	0.62
Anatase TiO_2 microsphere/PVB coating specimen	56.8	1569	4.39	0.64	3102	3.07	0.69
Rutile TiO_2 microsphere/PVB coating specimen	64.0	4823	3.44	0.73	48,130	3.89	0.77
Anatase TiO_2 nanosheet/PVB coating specimen	94.8	688	7.79	0.82	2254	2.82	0.65

when the copper and TiO_2 are both exposed to the solution, while rutile TiO_2 does not. In addition, the anatase TiO_2 nanosheets exhibit a more intense "corrosion-promotion activity" than the anatase TiO_2 microspheres.

The current distribution around the defect differs considerably from that in the coated area. However, traditional impedance techniques such as EIS measurement cannot easily separate these differences and always acquire overall impedance among the whole specimen. Therefore, LEIS measurement is used to better characterize the corrosion behavior of copper substrates at the defects. Fig. 4 shows the LEIS mappings at the artificial defects of the four scratched coated specimens. The color intensity characterizes the impedance distribution cross the test surface, in which the lowest impedance value is generated at the defect area on the coated electrode. As shown in Fig. 4**a** and **c**, the lowest impedance values at the defects of pure PVB coating specimen and rutile TiO_2 microsphere/PVB coating specimen are about $8.6 \times 10^3\ \Omega\ cm^2$ and $4.2 \times 10^3\ \Omega\ cm^2$, respectively, while those of anatase TiO_2 microsphere/PVB coating specimen and anatase TiO_2 nanosheet/PVB coating specimen are approximately $8.5 \times 10^2\ \Omega\ cm^2$ and $2.2 \times 10^2\ \Omega\ cm^2$ (Fig. 4**b** and **d**). It indicates that the impedance value at the artificial defect of rutile TiO_2 microsphere/PVB coating specimen is roughly 5 times larger than that of anatase TiO_2 microsphere/PVB coating specimen and 19 times larger than that of anatase TiO_2 nanosheet/PVB coating specimen. The LEIS results are consistent with the previous EIS results, which further confirms that the presence of anatase TiO_2 could greatly accelerate corrosion development of copper substrates and increase the local anodic activity at the scratch areas, while rutile TiO_2 does not accelerate the corrosion of copper substrates. It suggests that the crystal types and structures of TiO_2 materials have a significant influence on the exhibition of "corrosion-promotion activity", determining the corrosion influences of semiconductor fillers on metals.

For the initial corrosion process of the metal coupled with semiconductor fillers, electrons transfer from the metal substrate to the semiconductor/electrolyte interface, and then the electrons are consumed by the oxygen reduction reaction at the semiconductor/electrolyte interface. For the semiconductor fillers that possess "corrosion-promotion activity", the rates of electron transfer and consumption during the corrosion process tend to be greatly increased, thereby facilitating the progress of metal corrosion. Understanding the corrosion-promotion mechanism is not only helpful for investigating the fundamental interactions between semiconductors and metals, but more importantly beneficial for the selection of suitable anticorrosive fillers, or the development of self-healing anticorrosive coating systems by utilizing the corrosion-promotion effect of semiconductor fillers [35, 36]. According to the previous research [37], the electron transfer and consumption process is determined by the work function differences between metal and semiconductor fillers as well as the cathodic reaction activity including ORR catalytic activity of semiconductor fillers. Moreover, the electrical conductivity of semiconductor fillers is an important factor for electron conduction in the semiconductor fillers as well. Therefore, the corrosion-promotion effect of different TiO_2 materials on copper is explained from three aspects below: the relative values of the work function between copper and TiO_2 fillers, the electrical conductivity and oxygen reduction activity of different TiO_2 fillers.

3.3. SKP measurements

Scanning Kelvin probe method is an indirect technique for work function measurements, which measures the contact potential difference (CPD) between the sample surface and the probe. From the measured CPD, the effective work function of the samples can be calculated according to Hansen [52] using the following equation:

$$WF = e\Delta\phi + WF_0 \tag{2}$$

where WF and WF_0 are the respective work functions of the samples and the tungsten probe in eV, $\Delta\phi$ is the CPD between the sample surface and the probe in volt. The work function of the tungsten probe is 4.55 eV [53], which is taken as WF_0.

Fig. 5 shows the CPD mapping images of TiO_2 thin films with different crystal structures and copper. To further ensure the reliability of the CPD data and determine the CPD values, the histograms shown in Fig. 5 as inserts are fitted by Gaussian equation [47]:

$$y = y_0 + \frac{A}{\sigma\sqrt{\pi/2}}\exp\left[-\frac{2(x-\mu)^2}{\sigma^2}\right] \tag{3}$$

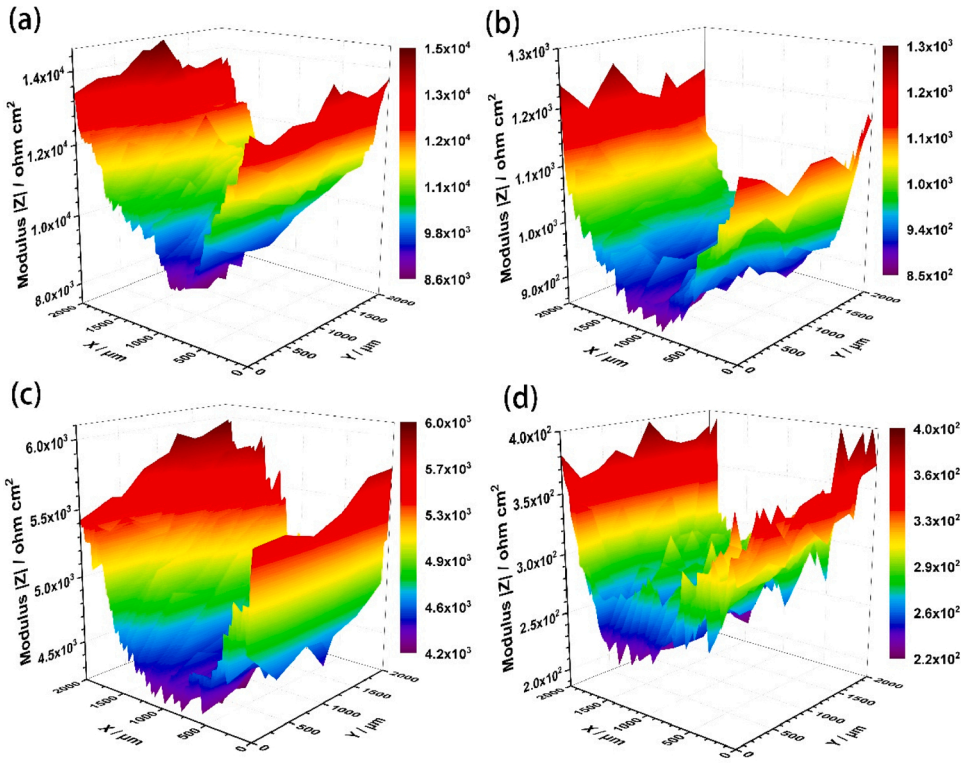

Fig. 4. LEIS mappings around the artificial defects of (a) pure PVB coating specimen, (b) anatase TiO_2 microsphere/PVB coating specimen, (c) rutile TiO_2 microsphere/PVB coating specimen and (d) anatase TiO_2 nanosheet/PVB coating specimen at a frequency of 1 Hz during 1 h of immersion in 3.5 wt.% NaCl aqueous solution.

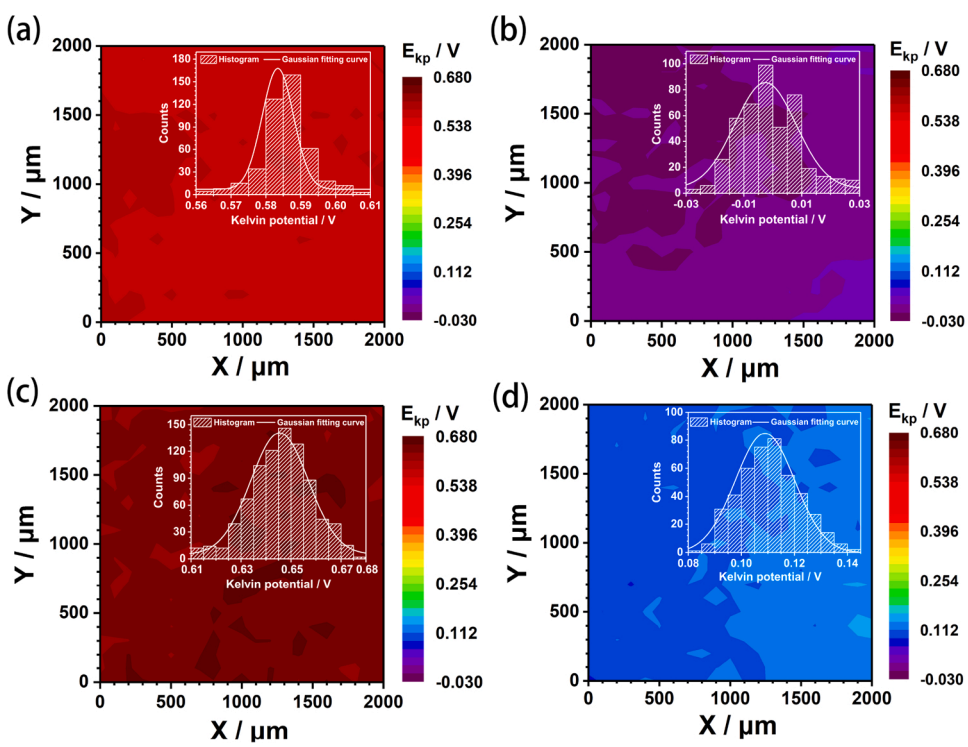

Fig. 5. CPD mapping images of (a) anatase TiO_2 microsphere, (b) rutile TiO_2 microsphere, (c) anatase TiO_2 nanosheet and (d) copper. Inset: the corresponding histograms and Gaussian fitting curves of CPD distribution for the samples.

where y_0 is the ordinate offset; A is a constant; μ is the expectation of Gaussian distribution, meaning the location of the peak value of the CPD; σ^2 is the variance of Gaussian distribution, meaning the degree of CPD dispersion among the whole measured surface. The values of parameters fitted by Eq. (3) are shown in Table 2. It can be observed that the dispersion of the measured CPD values is small for the four materials,

Table 2
Gaussian fitting parameters of CPD distribution and work functions for different TiO_2 materials and Cu.

Samples	μ	σ^2	Work function / eV
anatase TiO_2 microsphere	0.58	$(0.009)^2$	5.13
rutile TiO_2 microsphere	−0.01	$(0.019)^2$	4.54
anatase TiO_2 nanosheet	0.65	$(0.022)^2$	5.20
copper	0.11	$(0.023)^2$	4.66

indicating the uniformity of the sample surfaces and the reliability of measured CPD values. The measured values of μ (i.e. CPD) for anatase TiO_2 microsphere, rutile TiO_2 microsphere, anatase TiO_2 nanosheet and copper were 0.58, −0.01, 0.65 and 0.11, respectively, from which the work functions of the four samples could be calculated using Eq. (2). From Table 2, it can be seen that the work function of copper is higher than that of rutile TiO_2 but lower than that of anatase TiO_2. The work function difference between the two phases is the driving force of the electron transfer in their interface. When two phases come into a galvanic contact, the electrons tend to transfer from the phase with a lower work function to the other until their Fermi levels become equal. In general, a larger work function difference between two phases is more favorable for electron transfer process. According to the calculated work function values, it is more stable for the electrons staying in copper which has higher work function rather than rutile TiO_2 when the two phases come into contact. In contrast, the electrons tend to transfer from the copper to the two anatase TiO_2, resulting in the accelerated corrosion of copper. Moreover, the work function difference between anatase TiO_2 nanosheet and copper is larger than that between anatase TiO_2 microsphere and copper, leading to more severe corrosion of copper, which is consistent with the EIS and LEIS results.

3.4. Mott-Schottky analysis of different TiO_2 crystals

Mott–Schottky analysis was employed to determine the properties of different TiO_2 crystals, and the results are shown in Fig. 6. Mott–-Schottky plots of three samples show a positive slope, indicating that three TiO_2 materials are all n-type semiconductors. Owing to that the work function of copper is lower than those of two anatase TiO_2 materials and higher than that of rutile TiO_2 material, ohmic contact (n-type anti-blocking layer) can be formed at the copper/n-type anatase TiO_2 interface, where the electrons can easily transfer from copper substrate to anatase TiO_2, while Schottky contact (n-type blocking layer) formed at the copper/n-type rutile TiO_2 interface can prevent electrons from transferring from copper to the rutile TiO_2.

For an n-type semiconductor material, the relationship for Mott–-Schottky analysis can be expressed by the following equation:

$$\frac{1}{C^2} = \frac{2}{e\varepsilon\varepsilon_0 N_D}\left(E - E_{fb} - \frac{kT}{e}\right) \quad (4)$$

where C is the capacitance of the space charge layer in the semiconductor (F m^{-2}); N_D is the donor density (m^{-3}); e is the elemental charge (1.602×10^{-19} C); ε_0 is the permittivity of free space (8.854×10^{-12} F m^{-1}); ε is the relative permittivity of the semiconductor (ε = 31.0 for anatase [54], ε = 43.2 for rutile [55]); E is the applied potential (V); E_{fb} is the flat band potential (V); T is the absolute temperature (K) and k is the Boltzmann constant (1.380×10^{-23} J·K^{-1}). Based on Eq. (4) and Fig. 6, a linear dependence is expected, from whose slope the donor density can be obtained. The rutile TiO_2 exhibits a lower donor density ($N_D = 6.253 \times 10^{19}$ cm^{-3}) compared with the anatase TiO_2 microsphere ($N_D = 9.359 \times 10^{19}$ cm^{-3}) and anatase TiO_2 nanosheet ($N_D = 1.303 \times 10^{20}$ $cm^{-}\times^{3}$). The higher N_D would enhance electrical conductivity and reduce electron transfer resistance. Therefore, the high electrical conductivity of two anatase TiO_2 materials results in severe corrosion while the materials contact with copper.

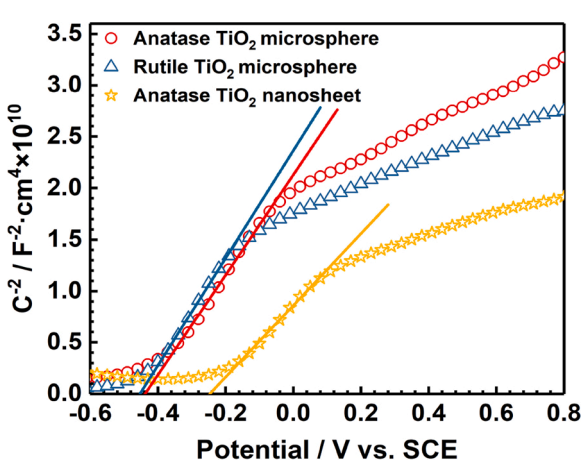

Fig. 6. Mott-Schottky plots of different TiO_2 crystals in 3.5 wt.% NaCl solution at a frequency of 1 kHz.

3.5. Oxygen reduction activity of different TiO_2 crystals

The ORR polarization curves of different TiO_2 crystals are shown in Fig. 7**a** and the corresponding results are listed in Table 3. The polarization curve of anatase TiO_2 nanosheet indicates an onset potential (the potential at the current density of −0.1 mA cm^{-2}) of −0.27 V vs. SCE and an obvious oxygen reduction peak around -0.46 V vs. SCE, whereas the onset potential of anatase TiO_2 microsphere and rutile TiO_2 microsphere shift negatively to −0.38 V and −0.47 V vs. SCE, respectively. The curve of anatase TiO_2 nanosheet shows the current density of 2.39 mA cm^{-2} at −1.0 V vs. SCE which is much higher than that of anatase TiO_2 microsphere (1.22 mA cm^{-2}) or rutile TiO_2 microsphere (0.85 mA cm^{-2}) at −1.0 V vs. SCE. The difference in the current densities at −1.0 V vs. SCE among the three materials suggests that anatase TiO_2 show higher ORR activity than rutile TiO_2. Moreover, this result is also in accord with the common belief that controlling the exposed {001} facet can effectively improve the catalytic ORR activity of TiO_2 materials [41]. The Tafel plots of ORR on different TiO_2 crystals are shown in Fig. 7**b**. The Tafel slope of the anatase TiO_2 nanosheet is calculated to 182 mV·dec^{-1}, which is smaller than that of the anatase TiO_2 microsphere (308 mV·dec^{-1}) or rutile TiO_2 microsphere (335 mV·dec^{-1}). This result indicates the anatase TiO_2 nanosheet has a higher transfer coefficient of ORR than the anatase TiO_2 microsphere or rutile TiO_2 microsphere in 3.5 wt.% NaCl solution, which agrees well with the above analysis of the ORR performance of different TiO_2 crystals. The higher ORR activity of semiconductor filler could increase the oxygen reduction rate in the solution, which promotes electron consumption. Therefore, when electrons transfer from copper substrate to the semiconductor filler with higher ORR activity, the ORR cathode reaction can occur continuously and rapidly, avoiding electron accumulation on the surface of the semiconductor filler. The above analysis suggests that the anatase TiO_2 nanosheet accelerates copper corrosion more intensely than the anatase TiO_2 microsphere or rutile TiO_2 microsphere.

3.6. Corrosion mechanism

To elaborate the reason why the different TiO_2 crystals behave different corrosion-promotion effect on copper, a mechanism based on the whole metal corrosion process, including the cathodic and anodic processes of corrosion reaction is proposed, as shown in Fig. 8. Considering that the corrosion of metals includes the process of electron transfer and consumption of metals, the mechanism describes the corrosion-promotion effect of different TiO_2 crystals on copper from three aspects: the work functions of copper and TiO_2, the electrical conductivity and ORR catalytic activity of TiO_2 materials.

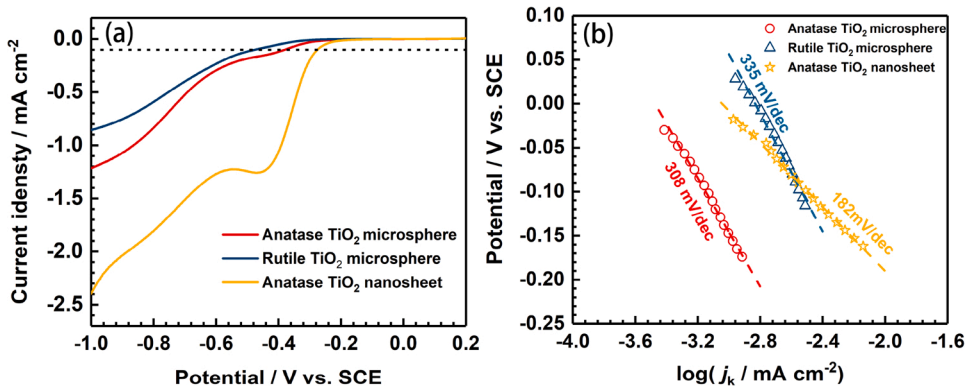

Fig. 7. (a) Linear sweeping voltammograms for different TiO_2 crystals on an RDE in an O_2-saturated 3.5 wt.% NaCl solution with a sweeping rate of 10 mV s^{-1} at a rotation rate of 1200 rpm; (b) Tafel plots of different TiO_2 crystals.

Table 3
Results for polarization curves of different TiO_2 crystals obtained from Fig. 7.

Samples	Onset potential[a] / V vs. SCE	Current density[b] / mA· cm^{-2}	Tafel slope / mV·dec^{-1}
anatase TiO_2 microsphere	−0.47	1.22	308
rutile TiO_2 microsphere	−0.38	0.85	335
anatase TiO_2 nanosheet	−0.27	2.39	182

[a] Onset potential: the potential at the current density of −0.1 mA· cm^{-2}.
[b] Current density: the current density at −1.0 V vs. SCE.

When the coated specimens are scratched, the copper substrate and TiO_2 are exposed to the corrosive electrolyte, as shown in Fig. 8. The corrosion rate of copper in contact with rutile TiO_2 filler is of the same magnitude as that of the copper at the scratch of pure PVB coating, while the two anatase TiO_2 fillers show a significant "corrosion-promotion activity". Since the relative magnitude of the work function of metal (W_m) and the work function of semiconductor material (W_s) determines the electron or charge transfer direction between metal and semiconductor material, the work function is chosen to describe the difference of "corrosion-promotion activity" between the anatase TiO_2 and rutile TiO_2. For the scratched anatase TiO_2 microsphere/PVB coating specimen and anatase TiO_2 nanosheet/PVB coating specimen, there are two paths for the corrosion of copper, as shown in Fig. 8**a**. One path is that oxygen is directly reduced on the copper surface, causing the copper corrosion. The explanation for the other corrosion path is described below: the work function of anatase TiO_2 is higher than that of copper, and an ohmic contact can be formed at the copper/n-type anatase TiO_2 interface, providing an electron tunneling pathway across the interface. Thus, the electrons can easily transfer from copper to anatase the TiO_2 until their Fermi levels become equal. The electron transfer results in the formation of an electrical barrier preventing further electron transfer. However, oxygen in the electrolyte is reduced at the anatase TiO_2/electrolyte interface, leading to the consumption of the accumulated electrons in the anatase TiO_2. Afterward, electrons in copper can flow continuously to the anatase TiO_2, accelerating the anodic reaction of the copper corrosion. In the latter path for copper corrosion, the cathodic and anodic reactions of the corrosion occur at different regions, thereby accelerating copper corrosion as well. In contrast, for the scratched rutile TiO_2 microsphere/PVB coating specimen, the n-type rutile TiO_2 has a lower work function than copper, leading to the formation of Schottky contact at the copper/n-type rutile TiO_2 interface, which prevents the electron from transferring from copper to rutile TiO_2. Hence, there is only one path for the corrosion of copper at the scratch of the rutile TiO_2 microsphere/PVB coating, as shown in Fig. 8b, which exhibits the same corrosion behavior as the copper at the scratch of the pure PVB coating.

As discussed above, both kinds of n-type anatase TiO_2 could open up a new corrosion path for the copper substrate, while there is still a significant difference in copper corrosion between the two anatase TiO_2

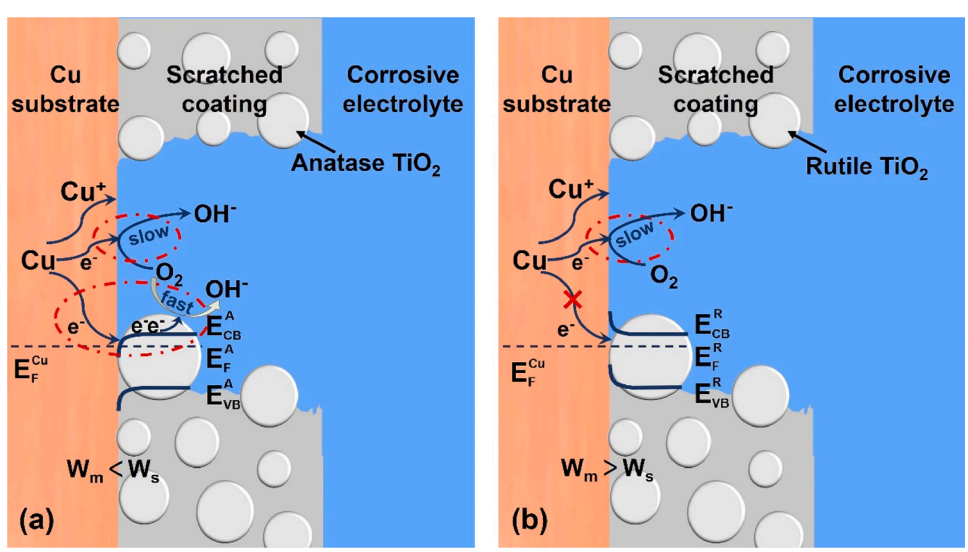

Fig. 8. Schematic of the mechanism for corrosion-promotion effect at (a) the Cu/anatase TiO_2/electrolyte, (b) the Cu/rutile TiO_2/electrolyte interfaces.

materials. This is related to the other two necessary factors which affect the electron conduction inside the semiconductor materials and the electron consumption at the semiconductor materials/electrolyte interface. The two factors ensure the electrons can be consumed continuously and rapidly by the cathodic reaction on the semiconductor materials. To meet the two factors, semiconductor materials need to exhibit high electrical conductivity and high catalytic activity for cathodic reactions, such as oxygen reduction reaction or hydrogen evolution reaction. As shown in Figs. 6 and 7, both the conductivity and the oxygen reduction activity of the anatase TiO_2 nanosheet are higher than those of the anatase TiO_2 microsphere, resulting in the anatase TiO_2 nanosheet exhibiting a higher "corrosion-promotion activity" than the anatase TiO_2 microsphere. The work provides knowledge of the essence of corrosion reaction between metal and semiconductor materials and a basis for the development and practical application of semiconductor materials in corrosion protection. However, it should be pointed out that our present understanding of the mechanism for "corrosion-promotion activity" in this work is only qualitative, and a quantitative study on the mechanism for "corrosion-promotion activity" is in progress.

4. Conclusions

In summary, three types of TiO_2 with different crystal structures were prepared and incorporated into PVB composite coatings. The influences of different TiO_2 materials on the initial corrosion behavior of copper at the defects in dark conditions have been studied through EIS and LEIS. The anatase TiO_2 exhibit intense "corrosion-promotion activity", while the rutile TiO_2 does not. A mechanism for "corrosion-promotion activity" is proposed basing on the whole corrosion process. Owing to the formation of the n-type anti-blocking layer formed at the metal/semiconductor filler interface, electrons can easily transfer from metal to semiconductor, accelerating the anodic reaction of corrosion process. Besides, the high oxygen reduction activity and high conductivity of semiconductors guarantee electrons being consumed continuously and rapidly, promoting the cathodic reaction of corrosion process. This mechanism is instructive for the basis of selecting semiconductor as anticorrosive fillers and the crystal structure design of semiconductor fillers. Moreover, since most of metal corrosion products behave semiconducting properties, the mechanism could also be used to study the influences of corrosion products on the subsequent corrosion behavior of metals, which could deepen our understanding of the nature of metal corrosion.

Data availability

The raw/processed data required to reproduce these findings cannot be shared at this time as the data also forms part of an ongoing study.

CRediT authorship contribution statement

Xinyu Zhang: Formal analysis, Investigation, Validation, Writing - original draft, Writing - review & editing. **Sijia Li:** Investigation, Writing - original draft. **Wen Sun:** Conceptualization, Resources, Writing - review & editing, Funding acquisition. **Lida Wang:** Resources, Writing - review & editing, Project administration, Funding acquisition. **Jing Wang:** Funding acquisition. **Guichang Liu:** Methodology, Supervision, Resources, Funding acquisition.

Declaration of Competing Interest

The authors declare that they have no known competing financial interests or personal relationships that could have appeared to influence the work reported in this paper.

Acknowledgments

This work was supported by National Natural Science Foundation of China (No. 21703026, 51671047, 21978036, 21403030), Key R&D Project of Ningxia Hui Autonomous Region (No. 2019BFG02016), China Postdoctoral Science Foundation (No. 2017M610177, 2018T110222), Research Fund of Open Studio for Marine Corrosion and Protection and Pilot National Laboratory for Marine Science and Technology (Qingdao, No. HYFSKF-201804), and Fundamental Research Funds for the Central Universities (No. DUT19RC(4)003).

References

[1] Y. He, Q. He, L. Wang, C. Zhu, P. Golani, A.D. Handoko, X. Yu, C. Gao, M. Ding, X. Wang, F. Liu, Q. Zeng, P. Yu, S. Guo, B.I. Yakobson, L. Wang, Z.W. Seh, Z. Zhang, M. Wu, Q.J. Wang, H. Zhang, Z. Liu, Self-gating in semiconductor electrocatalysis, Nat. Mater. 18 (2019) 1098–1104, https://doi.org/10.1038/s41563-019-0426-0.
[2] H. Zhang, R. Lv, Defect engineering of two-dimensional materials for efficient electrocatalysis, J. Mater. 4 (2018) 95–107, https://doi.org/10.1016/j.jmat.2018.02.006.
[3] W.T. Hong, M. Risch, K.A. Stoerzinger, A. Grimaud, J. Suntivich, Y. Shao-Horn, Toward the rational design of non-precious transition metal oxides for oxygen electrocatalysis, Energ. Environ. Sci. 8 (2015) 1404–1427, https://doi.org/10.1039/c4ee03869j.
[4] S. Ryu, M. Hoffmann, Mixed-metal semiconductor anodes for electrochemical water splitting and reactive chlorine species generation: implications for electrochemical wastewater treatment, Catalysts 6 (2016) 59, https://doi.org/10.3390/catal6040059.
[5] S.T. Kochuveedu, Y.H. Jang, D.H. Kim, A study on the mechanism for the interaction of light with noble metal-metal oxide semiconductor nanostructures for various photophysical applications, Chem. Soc. Rev. 42 (2013) 8467, https://doi.org/10.1039/c3cs60043b.
[6] M. Qiao, Y. Chen, Y. Wang, Y. Li, The germanium telluride monolayer: a two dimensional semiconductor with high carrier mobility for photocatalytic water splitting, J. Mater. Chem. A 6 (2018) 4119–4125, https://doi.org/10.1039/c7ta10360c.
[7] A. Paracchino, V. Laporte, K. Sivula, M. Grätzel, E. Thimsen, Highly active oxide photocathode for photoelectrochemical water reduction, Nat. Mater. 10 (2011) 456–461, https://doi.org/10.1038/nmat3017.
[8] N.K. Elumalai, C. Vijila, R. Jose, A. Uddin, S. Ramakrishna, Metal oxide semiconducting interfacial layers for photovoltaic and photocatalytic applications, Mater. Renew. Sust. Energ. 4 (2015) 1–25, https://doi.org/10.1007/s40243-015-0054-9.
[9] X. Wu, X. Huang, X. Qi, H. Li, B. Li, H. Zhang, Copper-based ternary and quaternary semiconductor nanoplates: templated synthesis, characterization, and photoelectrochemical properties, Angew. Chem. Int. Edit. 53 (2014) 8929–8933, https://doi.org/10.1002/ange.201403655.
[10] D. Wang, R. Kou, D. Choi, Z. Yang, Z. Nie, J. Li, L.V. Saraf, D. Hu, J. Zhang, G. L. Graff, J. Liu, M.A. Pope, I.A. Aksay, Ternary self-assembly of ordered metal oxide-graphene nanocomposites for electrochemical energy storage, ACS Nano 4 (2010) 1587–1595, https://doi.org/10.1021/nn901819n.
[11] B.L. Ellis, P. Knauth, T. Djenizian, Three-dimensional self-supported metal oxides for advanced energy storage, Adv. Mater 26 (2014) 3368–3397, https://doi.org/10.1002/adma.201306126.
[12] X. Peng, L. Peng, C. Wu, Y. Xie, Two dimensional nanomaterials for flexible supercapacitors, Chem. Soc. Rev. 43 (2014) 3303–3323, https://doi.org/10.1039/c3cs60407a.
[13] Y. Jing, Z. Zhou, C.R. Cabrera, Z. Chen, Graphene, inorganic graphene analogs and their composites for lithium ion batteries, J. Mater. Chem. A 2 (2014) 12104–12122, https://doi.org/10.1039/c4ta01033g.
[14] C. Tan, H. Zhang, Two-dimensional transition metal dichalcogenide nanosheet-based composites, Chem. Soc. Rev. 44 (2015) 2713–2731, https://doi.org/10.1039/c4cs00182f.
[15] E. Yoo, J. Kim, E. Hosono, H. Zhou, T. Kudo, I. Honma, Large reversible Li storage of graphene nanosheet families for use in rechargeable lithium ion batteries, Nano Lett. 8 (2008) 2277–2282, https://doi.org/10.1021/nl800957b.
[16] S.O. Pehkonen, S. Yuan, The inorganic film coatings for corrosion protection. Interface Science and Technology, Elsevier, 2018, pp. 185–255, https://doi.org/10.1016/B978-0-12-813584-6.00007-7.
[17] A.G. Scheuermann, P.C. McIntyre, Atomic layer deposited corrosion protection: a path to stable and efficient photoelectrochemical cells, J. Phys. Chem. Lett. 7 (2016) 2867–2878, https://doi.org/10.1021/acs.jpclett.6b00631.
[18] W. Sun, Investigation on the Corrosion Protection Performance of Two-dimensional material/polymer Composite Coatings (in Chinese), Dalian University of Technology, 2016, p. 166.
[19] Z. Yang, W. Sun, L. Wang, S. Li, T. Zhu, G. Liu, Liquid-phase exfoliated fluorographene as a two dimensional coating filler for enhanced corrosion protection performance, Corros. Sci. 103 (2016) 312–318, https://doi.org/10.1016/j.corsci.2015.10.039.
[20] S. Ren, M. Cui, W. Li, J. Pu, Q. Xue, L. Wang, N-doping of graphene: toward long-term corrosion protection of Cu, J. Mater. Chem. A 6 (2018), https://doi.org/10.1039/c8ta05421e.

[21] J. Ding, H. Zhao, D. Ji, B. Xu, X. Zhao, Z. Wang, D. Wang, Q. Zhou, H. Yu, Achieving long-term anticorrosion via the inhibition of graphene's electrical activity, J. Mater. Chem. A 7 (2019) 2864–2874, https://doi.org/10.1039/c8ta10337b.

[22] J. Ding, H. Zhao, X. Zhao, B. Xu, H. Yu, How semiconductor transition metal dichalcogenides replaced graphene for enhancing anticorrosion, J. Mater. Chem. A 7 (2019) 13511–13521, https://doi.org/10.1039/c9ta04033a.

[23] K. Ollik, M. Rybarczyk, J. Karczewski, M. Lieder, Fabrication of anti-corrosion nitrogen doped graphene oxide coatings by electrophoretic deposition, Appl. Surf. Sci. 499 (2020), 143914, https://doi.org/10.1016/j.apsusc.2019.143914.

[24] H. Tang, Z. Qu, L. Wang, H. Ye, X. Fan, G. Zhang, Liquid-phase exfoliated SnS as a semiconductor coating filler to enhance corrosion protection performance, Phys. Chem. Chem. Phys. 21 (2019) 18179–18187, https://doi.org/10.1039/c9cp03381e.

[25] S. Radhakrishnan, C.R. Siju, D. Mahanta, S. Patil, G. Madras, Conducting polyaniline-nano-TiO_2 composites for smart corrosion resistant coatings, Electrochim. Acta 54 (2009) 1249–1254, https://doi.org/10.1016/j.electacta.2008.08.069.

[26] J. Miklecic, S.L. Blagojevic, M. Petric, V. Jirous-Rajkovic, Influence of TiO_2 and ZnO nanoparticles on properties of waterborne polyacrylate coating exposed to outdoor conditions, Prog. Org. Coat. 89 (2015) 67–74, https://doi.org/10.1016/j.porgcoat.2015.07.016.

[27] T. Jin, F. Kong, R. Bai, R. Zhang, Anti-corrosion mechanism of epoxy-resin and different content Fe_2O_3 coatings on magnesium alloy, Front. Mater. Sci. 10 (2016) 367–374, https://doi.org/10.1007/s11706-016-0357-5.

[28] J. Chen, K. Huang, S. Liu, Hydrothermal preparation of a protective Fe_3O_4 film on Fe foil, Corros. Sci. 50 (2008) 1982–1986, https://doi.org/10.1016/j.corsci.2008.05.002.

[29] R. Subasri, T. Shinohara, K. Mori, TiO_2-based photoanodes for cathodic protection of copper, J. Electrochem. Soc. 152 (2005) B105–B110, https://doi.org/10.1149/1.1856912.

[30] H. Deng, M. Huang, W. Weng, J. Lin, Photocathodic protection of iron oxide nanotube arrays fabricated on carbon steel, Surf. Coat. Technol. 266 (2015) 183–187, https://doi.org/10.1016/j.surfcoat.2015.02.042.

[31] R. Subasri, T. Shinohara, Investigations on SnO_2–TiO_2 composite photoelectrodes for corrosion protection, Electrochem. Commun. 5 (2003) 897–902, https://doi.org/10.1016/j.elecom.2003.08.016.

[32] Y. Bu, J. Ao, A review on photoelectrochemical cathodic protection semiconductor thin films for metals, Green Energy Environ. 2 (2017) 331–362, https://doi.org/10.1016/j.gee.2017.02.003.

[33] M. Sun, Z. Chen, Y. Bu, J. Yu, B. Hou, Effect of ZnO on the corrosion of zinc, Q235 carbon steel and 304 stainless steel under white light illumination, Corros. Sci. 82 (2014) 77–84, https://doi.org/10.1016/j.corsci.2013.12.022.

[34] M. Li, S. Luo, P. Wu, J. Shen, Photocathodic protection effect of TiO_2 films for carbon steel in 3% NaCl solutions, Electrochim. Acta 50 (2005) 3401–3406, https://doi.org/10.1016/j.electacta.2004.12.031.

[35] W. Sun, L. Wang, T. Wu, G. Liu, α-Mn_2O_3-catalyzed adsorption reaction of benzotriazole for "smart" corrosion protection of copper, Corros. Sci. 82 (2014) 1–6, https://doi.org/10.1016/j.corsci.2014.01.001.

[36] W. Sun, L. Wang, T. Wu, T. Zhu, H. Xie, Y. Pan, G. Liu, A catalyst-based self-sufficient system with durable self-healing functionality, Adv. Eng. Mater. 18 (2016) 923–931, https://doi.org/10.1002/adem.201500494.

[37] S. Li, W. Sun, Z. Yang, X. Zhang, L. Wang, G. Liu, Influences of semiconductor oxide fillers on the corrosion behavior of metals under coatings, Electrochim. Acta 292 (2018) 425–434, https://doi.org/10.1016/j.electacta.2018.08.116.

[38] U. Diebold, The surface science of titanium dioxide, Surf. Sci. Rep. 48 (2003) 53–229, https://doi.org/10.1016/s0167-5729(02)00100-0.

[39] Z. Yin, S. Betzler, T. Sheng, Q. Zhang, X. Peng, J. Shangguan, K. Bustillo, J. Li, S. Sun, H. Zheng, Visualization of facet-dependent pseudo-photocatalytic behavior of TiO_2 nanorods for water splitting using in situ liquid cell TEM, Nano Energy (2019), https://doi.org/10.1016/j.nanoen.2019.05.068.

[40] S. Kashiwaya, J. Morasch, V. Streibel, T. Toupance, W. Jaegermann, A. Klein, The work function of TiO_2, Surfaces 1 (2018) 73–89, https://doi.org/10.3390/surfaces1010007.

[41] D. Pei, L. Gong, A. Zhang, X. Zhang, J. Chen, Y. Mu, H. Yu, Defective titanium dioxide single crystals exposed by high-energy {001} facets for efficient oxygen reduction, Nat. Commun. 6 (2015), https://doi.org/10.1038/ncomms9696.

[42] D. Dambournet, I. Belharouak, K. Amine, Tailored preparation methods of TiO_2 anatase, rutile, brookite: mechanism of formation and electrochemical properties, Chem. Mater. 22 (2009) 1173–1179, https://doi.org/10.1021/cm902613h.

[43] K. Chen, Z. Jiang, J. Qin, Y. Jiang, R. Li, H. Tang, X. Yang, Synthesis and improved photocatalytic activity of ultrathin TiO_2 nanosheets with nearly 100% exposed (001) facets, Ceram. Int. 40 (2014) 16817–16823, https://doi.org/10.1016/j.ceramint.2014.07.050.

[44] F. Karakaş, B.V. Hassas, M.S. Celik, Effect of precipitated calcium carbonate additions on waterborne paints at different pigment volume concentrations, Prog. Org. Coat. 83 (2015) 64–70, https://doi.org/10.1016/j.porgcoat.2015.02.003.

[45] R. Ashiri, A. Nemati, M. Sasani Ghamsari, Crack-free nanostructured $BaTiO_3$ thin films prepared by sol-gel dip-coating technique, Ceram. Int. 40 (2014) 8613–8619, https://doi.org/10.1016/j.ceramint.2014.01.078.

[46] C.D. Grill, J.P. Kollender, A.W. Hassel, Combinatorial electrodeposition of cobalt-copper material libraries, J. Electrochem. Soc. 163 (2016) D3069–D3075, https://doi.org/10.1149/2.0101612jes.

[47] M. Sun, K. Xiao, C. Dong, X. Li, P. Zhong, Electrochemical and initial corrosion behavior of ultrahigh strength steel by scanning Kelvin probe, J. Mater. Eng. Perform. 22 (2013) 815–822, https://doi.org/10.1007/s11665-012-0335-8.

[48] B. Liu, E.S. Aydil, Anatase TiO_2 films with reactive {001} facets on transparent conductive substrate, Chem. Commun. 47 (2011) 9507–9509, https://doi.org/10.1039/c1cc12365c.

[49] H.G. Yang, C.H. Sun, S.Z. Qiao, J. Zou, G. Liu, S.C. Smith, H.M. Cheng, G.Q. Lu, Anatase TiO_2 single crystals with a large percentage of reactive facets, Nature 453 (2008) 638–641, https://doi.org/10.1038/nature06964.

[50] H.G. Yang, G. Liu, S.Z. Qiao, C.H. Sun, Y.G. Jin, S.C. Smith, J. Zou, H.M. Cheng, G.Q.M. Lu, Solvothermal synthesis and photoreactivity of anatase TiO_2 nanosheets with dominant {001} facets, J. Am. Chem. Soc. 131 (2009) 4078–4083, https://doi.org/10.1021/ja808790p.

[51] D. Zhang, G. Li, X. Yang, J.C. Yu, A micrometer-size TiO_2 single-crystal photocatalyst with remarkable 80% level of reactive facets, Chem. Commun. (2009) 4381, https://doi.org/10.1039/b907963g.

[52] W.N. Hansen, G.J. Hansen, Standard reference surfaces for work function measurements in air, Surf. Sci. 481 (2001) 172–184.

[53] D. Lide, W. Haynes, CRC Handbook of Chemistry and Physics: a Ready-reference Book of Chemical and Physical Data, 90th edition, Fla.: CRC Press, Boca Raton, 2009, https://doi.org/10.5860/choice.37-4225.

[54] H. Tang, K. Prasad, R. Sanjines, P.E. Schmid, F. Levy, Electrical and optical properties of TiO_2 anatase thin films, J. Appl. Phys. 75 (1994) 2042–2047, https://doi.org/10.1063/1.356306.

[55] A. Wypych, I. Bobowska, M. Tracz, A. Opasinska, S. Kadlubowski, A. Krzywania-Kaliszewska, J. Grobelny, P. Wojciechowski, Dielectric properties and characterisation of titanium dioxide obtained by different chemistry methods, J. Nanomater 2014 (2014), https://doi.org/10.1155/2014/124814.